Nanoscale Advances

PAPER

View Article Online
View Journal | View Issue

Check for updates

Cite this: *Nanoscale Adv.*, 2019, **1**, 3212

A Ag nanoparticle functionalized Sg-C_3N_4/Bi_2O_3 2D nanohybrid: a promising visible light harnessing photocatalyst towards degradation of rhodamine B and tetracycline†

Sandip Padhiari and G. Hota *

Received 20th March 2019
Accepted 2nd July 2019

DOI: 10.1039/c9na00172g

rsc.li/nanoscale-advances

In the present work, S doped graphitic carbon nitride (Sg-C_3N_4) 2D nanosheets were synthesized by performing a thermal polymerization reaction of thiourea at 500 °C. After that the surface of Sg-C_3N_4 was functionalized with Bi_2O_3/Ag composite nanoparticles *via* a chemical precipitation method followed by heat treatment at 330 °C. The prepared Sg-C_3N_4/Bi_2O_3/Ag ternary nanocomposites were used as a visible light active photocatalyst for catalytic degradation of rhodamine B (RhB) dye and tetracycline hydrochloride, under natural solar light. The prepared ternary nanocomposites were characterized by using UV-Vis DRS, FT-IR, FESEM, EDX, TEM, XRD, photoluminescence (PL), electrochemical impedance spectroscopy and XPS analytical techniques. The XRD, UV-Vis DRS and FT-IR studies clearly revealed the formation of ternary phases in the composites. From the TEM and EDX studies it was clearly observed that spherical Ag nanoparticles (5–10 nm) and irregular Bi_2O_3 particles (60–120 nm) were decorated on the surface of 2D S doped g-C_3N_4 nanosheets. XPS studies also confirmed the formation of the ternary nanocomposite system. The results from the photocatalytic degradation of RhB dye revealed that 95% of the RhB dye was decolorized within 90 min of contact time by Sg-C_3N_4/Bi_2O_3/Ag ternary nanocomposites under natural solar light. Among the different prepared photocatalysts, Sg-C_3N_4/Bi_2O_3/Ag (15%) was found to be the most efficient photocatalyst towards the decolourization of RhB dye. This result is ascribed to the optimum loading of Ag, formation of a hetero-junction between the ternary phases, more light harvesting capacity and the lowest recombination rate of charge carriers. Apart from the coloured RhB dye, the photocatalytic degradation of the non-coloured tetracycline hydrochloride (TCH) compound was also studied to understand the photosensitization effect on the degradation process. Again scavenger studies were also performed in order to understand the mechanism of photodegradation. It was observed that along with the electron and hole pairs generated by light photons, hydroxide radicals play an important role in the degradation mechanism. The reusability study indicates that the photocatalysts prepared were highly stable at room temperature and can be recycled and reused for up to four successful cycles without a major loss in their performance.

1. Introduction

The energy crisis and environmental water pollution are the two major problems that restricted the sustainable growth of the human race in last few decades. Among the various methods adopted to overcome these problems, semiconductor based visible light photocatalysis is proven to be the most effective method as it utilises renewable solar energy and generates less harmful products during the photocatalytic degradation process.[1] Natural sunlight consists of 48% visible light and less than 5% UV light so there is an urgent need for the development of photocatalysts that could efficiently utilise the maximum solar energy.[2] Nano-sized semiconductors, such as TiO_2,[3–5] ZnO,[6–8] Ag_2O,[9] SnO_2,[10] and $BiVO_4$,[11] are the most widely investigated heterogeneous photocatalytic materials. But unfortunately, the photocatalytic performances of all these materials using visible light are far from our expectations. Recent research has focused on the development of graphitic carbon nitride (g-C_3N_4) based photocatalyst materials. g-C_3N_4 being a metal free organic semiconducting material with a unique two dimensional (2D) structure, suitable band gap

---

Department of Chemistry, NIT, Rourkela, Odisha, India, 769008. E-mail: garud@nitrkl.ac.in; garud31@yahoo.com; Fax: +91-661-2462022; Tel: +91-661-2462655

† Electronic supplementary information (ESI) available: The schematic procedure for the synthesis of the g-C_3N_4/Bi_2O_3/Ag ternary nanocomposite, reusability study for degradation of RhB and the XRD pattern of the Sg-C_3N_4/Bi_2O_3/Ag (15%) photocatalyst before and after photocatalytic reaction, k_{app} values for degradation of RhB and TCH on different prepared photocatalysts, and percentage of degradation of RhB in the presence of different trapping reagents. See DOI: 10.1039/c9na00172g

(2.7 eV), exceptional thermodynamic and chemical stability has attracted recent research attention.[9,12–14] However, like other metal oxide semiconductor based photocatalysts, it also suffers from limitations such as a high rate of recombination of photo induced charge carriers and low absorbance above 460 nm, which limit its practical applications in the field of visible light photocatalysis.[15–17] In order to overcome these limitations various structural and surface modification strategies have been adopted in recent years such as doping with non-metals or metals,[18,19] developing different g-C_3N_4 nanostructures with different morphologies and porosity, creating hetero-junctions with other semiconducting materials, deposition of noble metals,[20–23] and coupling with carbonaceous[12,24] materials.

Among the various structural modification methods, doping with metals (*e.g.*, Fe, Co, K, and Cu)[25–28] or non-metals (*e.g.*, B, C, S, P and Br)[29–33] can not only alter the electronic structure of g-C_3N_4 but also increase the defect structures as well as the surface active sites and hence improves the catalytic activity dramatically. In particular, it is reported that when g-C_3N_4 is doped with S, a new electron occupied energy level is formed slightly above the VB of pristine g-C_3N_4 due to the interaction of 3P states of S and 2P states of N which results in narrowing of the band gap and hence an increase in its visible light absorption capacity.[34,35] For example, Gang *et al.* in 2010 have reported the synthesis of S-doped g-C_3N_4 by heating pure g-C_3N_4 in the presence of a gaseous H_2S atmosphere at 450 °C. The obtained S-doped g-C_3N_4 photocatalyst was found to exhibit improved H_2 evolution capacity under visible light.[34] The synthetic method used produced a large amount of poisonous gases and hence was not considered as an environmentally friendly method. Recently, an eco-friendly approach for the synthesis of S doped g-C_3N_4 has been reported by using thiourea as the precursor which showed enhanced photocatalytic properties under visible light irradiation.[36]

Apart from the doping strategy, constructing a hetero-junction with other semiconductor nanomaterials, such as TiO_2,[13] Ag_2O,[9] CdS,[37] Ag_3PO_4,[38] and Fe_2O_3,[5] facilitates separation of electron–hole charge carriers and increases the light harvesting capacity of the resultant composites. Among different types of metal oxides, Bi_2O_3 is the most frequently studied metal oxide visible light responsive photocatalyst because it has a band gap of 2.8 eV which falls in the visible region of the light spectrum and it can also be prepared easily from low cost materials. But the main problem of α-Bi_2O_3 is that its valence band potential (VB) is sufficiently positive but its conduction band potential (CB) is not negative enough to reduce the surface O_2 to O_2^- ions through a rapid single electron reduction process and as a result photo-induced electron hole pairs recombine quickly and hence its photocatalytic activity decreases.[39–41]

On the other hand, noble metals such as Ag nanoparticles have attracted remarkable research interest because these metal nanoparticles exhibit the surface plasmon resonance (SPR) effect due to which they can strongly absorb visible light and can also improve the separation of electron and hole pairs on the semiconductor surface.[2,16,20,42–44] Furthermore, Ag based photocatalysts are economically more viable due to their relatively low price compared to other noble metals. Thus constructing a hetero-junction that contains S doped g-C_3N_4, Bi_2O_3 and Ag can generate a system that will not only increase interfacial boundary formation which is beneficial for the efficient separation of photo-generated electron hole pairs but can also extend the range of optical absorption in the visible region.

In the present study we have synthesized binary Bi_2O_3/Ag nanocomposites mounted on an S doped g-C_3N_4 2D nanosheet surface by using a simple chemical precipitation method followed by calcination at 330 °C. The prepared ternary Sg-C_3N_4/Bi_2O_3/Ag nanocomposites were characterized by XRD, FTIR, FESSM, TEM, XPS, PL, UV-vis DRS, and electrochemical study. The photocatalytic properties of the prepared ternary nanocomposites were investigated by catalytic degradation of rhodamine B (RhB) and tetracycline hydrochloride (TCH) under natural sunlight. The obtained results demonstrate that upon introduction of Ag into Sg-C_3N_4/Bi_2O_3 the photocatalytic activity of the resultant composite increases significantly. Furthermore, the mechanism of the degradation process has been studied in detail. The mechanistic pathway is well explained by means of scavenger studies and the reactive species involved in the degradation process is established from the respective confirmatory tests.

2. Materials and methods

2.1. Reagents used

Analytical grade thiourea, bismuth nitrate pentahydrate ($Bi(NO_3)_3 \cdot 5H_2O$), silver nitrate ($AgNO_3$), sodium hydroxide (NaOH), nitric acid (HNO_3), rhodamine B, tetracycline hydrochloride (TCH), benzoquinone, DMSO, EDTA, *tert*-butyl alcohol, terephthalic acid (TA), dichloro methane (DCM), and nitroblue tetrazolium chloride were purchased from Merck India and Himedia Lab. Pvt. Ltd. and were used without any purification. Deionised water was used throughout the experiments.

2.2. Preparation of photocatalysts

S doped g-C_3N_4 was prepared by heating thiourea in air at 500 °C with the help of an alumina crucible covered with a lid for 2 h. After synthesizing S doped g-C_3N_4, the ternary Sg-C_3N_4/Bi_2O_3/Ag nanocomposites were prepared by using the following procedure: typically 0.075 g of $Bi(NO_3)_3 \cdot 5H_2O$ was added to 30 ml of 1.5 M aqueous solution of nitric acid for preventing hydrolysis of Bi^{3+} ions. Then 0.5 g of Sg-C_3N_4 was added to it with magnetic stirring for 2 h so that all the Bi^{3+} ions will be completely adsorbed on the surface of Sg-C_3N_4. After that different amounts of $AgNO_3$ solution were added dropwise to the above suspension and the mixture was stirred for 30 min in the dark. Then KOH solution (50% w/v) was added gradually to it followed by continuous stirring until the solution pH reached 13 at which a yellow colour precipitate was formed. Then the resulting suspension was heated at 80 °C for 2 h. The obtained product was washed with ethanol and deionised water repeatedly several times. Finally, the solid product obtained was dried in an air oven, and then calcined at 330 °C for 2 h to get the ternary Sg-C_3N_4/Bi_2O_3/Ag nanocomposites. For comparison a series of Sg-C_3N_4/Bi_2O_3/Ag nanocomposites were prepared by varying the weight percentage of Ag ions, ranging from 5% to 20%. Pure Sg-C_3N_4/Bi_2O_3 was also prepared by using the above procedure without $AgNO_3$ addition. Scheme 1 shows the synthetic procedure for preparation of Sg-C_3N_4/Bi_2O_3/Ag ternary nanocomposites.

2.3. Photocatalytic degradation test

Rhodamine B (RhB) was taken as a model pollutant to study the photocatalytic properties of the synthesized Sg-C_3N_4/Bi_2O_3Ag composites. The photocatalytic degradation tests were performed under natural sunlight during the months of September and October, when the average light intensity was 82 600 lx. In a typical run 60 mg of catalyst was added to 70 ml of 15 ppm rhodamine B solution taken in a beaker. Before the photocatalytic degradation the solution was stirred for 60 min in the dark in order to examine the adsorptive removal of RhB dye onto the photocatalyst surface. After light illumination at every 15 min, 3 ml of the sample was taken out from the reaction mixture and the suspended photocatalyst was separated by centrifugation at room temperature. The RhB concentration in the solution was determined by measuring the absorbance at 554 nm with the help of a UV-Vis spectrophotometer. Different trapping agents such as dimethyl sulfoxide (DMSO), *p*-benzoquinone (p-BQ), tertiary butyl alcohol (TBA), and disodium ethylenediaminetetraacetate (2Na-EDTA) were used to detect the respective reactive species, such as electrons, superoxides, hydroxyl radicals, and holes, involved in the decolorization process. The concentration of each trapping reagent used was 1 mM. For all the photocatalytic studies, similar reaction conditions were maintained. The stability of the concerned most efficient photocatalyst was also investigated after the experiment by separating, washing several times with ethanol and double distilled water and then reusing the photocatalyst. Furthermore, since colour substances suffer from the photosensitisation effect, in order to examine the inherent photocatalytic ability of our synthesized photocatalysts, we have also performed the degradation of 10 ppm tetracycline hydrochloride (TCH) under similar conditions by using the same procedure.

2.4. Characterization technique

The crystallinity and phase purity of the synthesized ternary Sg-C_3N_4/Bi_2O_3/Ag nanocomposites were analyzed using a multipurpose X-ray diffraction system (Rigaku, Ultima-IV) under Ni-filtered CuKα ($\lambda = 1.5418$ Å) radiation. Chemical transformation of the synthesized composites was analysed by FTIR study by using a PerkinElmer infrared spectrometer (Perkin). A Jasco V-650 spectrometer in diffuse reflectance mode with $BaSO_4$ as a reference material was used to measure the UV-Vis spectra in the wavelength range from 200 to 800 nm. The photoluminescence analysis was performed using a Horiba Scientific spectrofluorimeter (Fluoromax-4) at an excitation wavelength of 380 nm. The morphology and microstructure of the photocatalysts were analysed using FESEM (Nova NanoSEM FEI microscope) and HRTEM (Tecnai 300 kV) analytical techniques. A PHI 5000 versa probe III instrument was used to perform the XPS analysis of the synthesised sample. Electro-chemical analysis was carried out using an electrochemical analyser (PSM, 1735) equipped with a three-electrode system in which a platinum wire was used as the counter electrode and an Ag/AgCl electrode was used as the reference electrode and 0.1 M Na_2SO_4 aqueous solution was the electrolyte. The degradation products of TCH were analyzed by GC-MS (Agilent GC 7980B) using a DB-1MS (30 m × 0.25 mm × 0.25 μm) column with helium (He) as the carrier gas. The photocatalytically degraded solution was extracted 3 times by using 15 ml DCM and reduced to 2 ml using a rotary evaporator prior to the GCMS study. The toxicity of TCH and its degradation products obtained during the photocatalytic reaction was determined *via* an antibacterial study, using an *E. coli* bacterial strain.

3. Results and discussion

3.1. XRD analysis

Crystallinity, phase purity and structural characteristics of the synthesized photocatalysts were determined *via* powder XRD analysis. Fig. 1 shows the XRD patterns of Sg-C_3N_4, Sg-C_3N_4/Bi_2O_3 and Sg-C_3N_4/Bi_2O_3/Ag nanocomposites containing different weight percentages (wt%) of Ag. For pure Sg-C_3N_4 two characteristic peaks were observed at $2\theta = 13.9°$ and 27.3° which are attributed to its (100) and (002) crystalline planes (JCPDS 87-1526). The former peak ($2\theta = 13.9°$) with much lower intensity

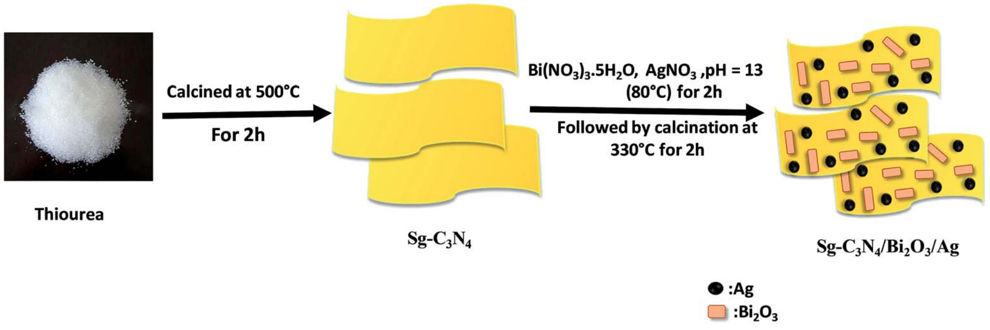

Scheme 1 Schematic route for the synthesis of Sg-C_3N_4/Bi_2O_3/Ag ternary photocatalysts.

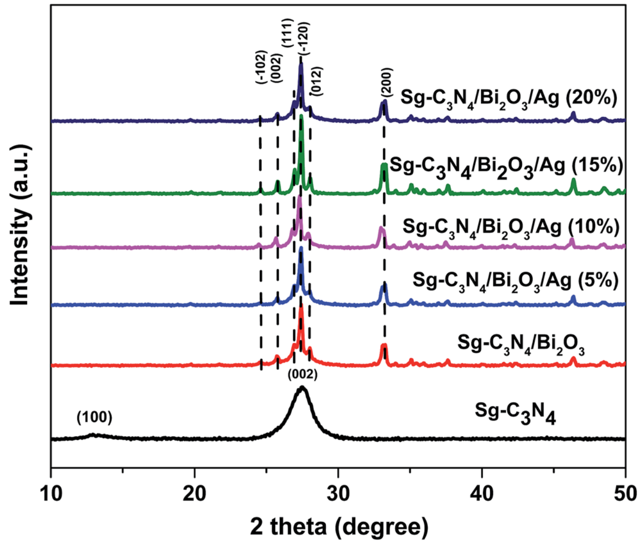

Fig. 1 XRD patterns of Sg-C_3N_4, Sg-C_3N_4/Bi_2O_3, Sg-C_3N_4/Bi_2O_3/Ag (5%), Sg-C_3N_4/Bi_2O_3/Ag (10%), Sg-C_3N_4/Bi_2O_3/Ag (15%), and Sg-C_3N_4/Bi_2O_3/Ag (20%).

corresponds to the in-plane structural packing motifs of the aromatic systems and the latter one with higher intensity corresponds to the inter-planar stacking of aromatic systems.[45,46] In the Sg-C_3N_4/Bi_2O_3 sample several diffraction peaks at $2\theta = 24.55$, 25.751, 26.949, 27.385, 28.038, and 33.27° were observed which are indexed to (−102), (002), (111), (−120), (012), and (200) crystal planes of monoclinic Bi_2O_3 and match well with JCPDS 14-0699. Further for Sg-C_3N_4/Bi_2O_3/Ag ternary nanocomposites all the peaks due to monoclinic Bi_2O_3 are only seen and no characteristic peaks for Sg-C_3N_4 and Ag are observed.[2,44] The absence of characteristic peaks for Ag in the ternary nanocomposites may be due to the high dispersity of low content ultra-small Ag nanoparticles over the surface of Sg-C_3N_4. Moreover, apart from the Bi_2O_3 peaks no other impurity peaks are observed which indicates that our samples are pure and no secondary phases are present in the synthesized samples.

3.2. FTIR analysis

FT-IR analysis was performed to obtain information on the existence of Sg-C_3N_4 in the synthesized composites. Fig. 2 shows the FTIR spectra of Sg-C_3N_4, Sg-C_3N_4/Bi_2O_3 and Sg-C_3N_4/Bi_2O_3/Ag nanocomposite photocatalysts containing different wt% of Ag. For all the samples a broad peak is observed within 3000–3500 cm^{-1} which is due to N–H stretching vibration of free amine groups present on the surface of Sg-C_3N_4 (ref. 47) and O–H stretching vibration of physically adsorbed water molecules.[48] The strong absorption band around 1250–1650 cm^{-1} with characteristic peaks at 1238, 1325, 1412, 1572, and 1625 cm^{-1} corresponds to the typical stretching vibration of the CN unit of the Sg-C_3N_4 heterocyclic ring. Again the bands visualised at 805 and 885 cm^{-1} are attributed to the breathing mode vibration of triazine units.[49] From the figure it is interesting to note that the intensity of the peak observed at 805 cm^{-1} gradually decreases with an increase in the amount of Ag in the ternary composite.

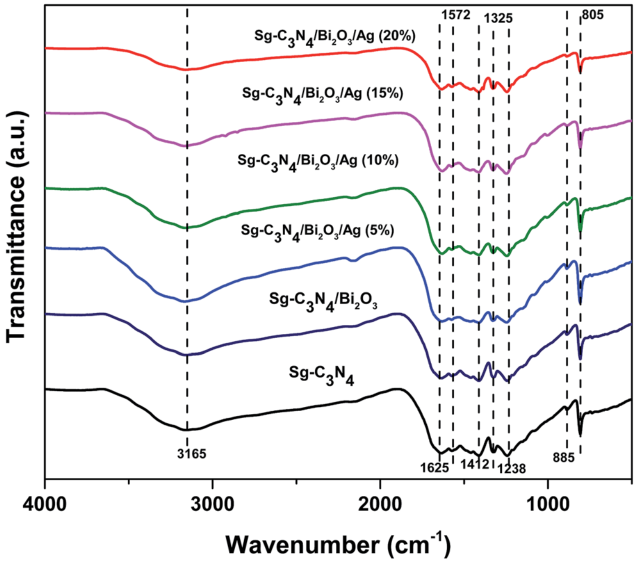

Fig. 2 FT-IR spectra of Sg-C_3N_4, Sg-C_3N_4/Bi_2O_3, Sg-C_3N_4/Bi_2O_3/Ag (5%), Sg-C_3N_4/Bi_2O_3/Ag (10%), Sg-C_3N_4/Bi_2O_3/Ag (15%), and Sg-C_3N_4/Bi_2O_3/Ag (20%).

3.3. Optical properties

3.3.1. PL study. A photoluminescence (PL) study of the photocatalytic material provides information on the migration, transfer, and separation efficiency of photo-induced charge carriers. Generally, it was observed that as the recombination rate of charge carrier decreases, the PL emission intensity decreases, which indicates improved separation of photogenerated electron–hole pairs. The PL emission spectra of Sg-C_3N_4/Bi_2O_3 and Sg-C_3N_4/Bi_2O_3/Ag nanocomposites excited with a wavelength of 380 nm at room temperature are presented in Fig. 3. From this figure, a strong emission peak centred at 430

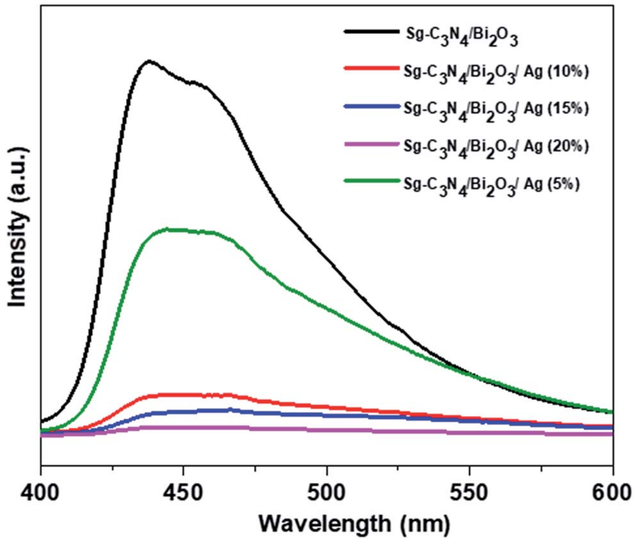

Fig. 3 Photoluminescence spectra of Sg-C_3N_4/Bi_2O_3, Sg-C_3N_4/Bi_2O_3/Ag (5%), Sg-C_3N_4/Bi_2O_3/Ag (10%), Sg-C_3N_4/Bi_2O_3/Ag (15%), and Sg-C_3N_4/Bi_2O_3/Ag (20%).

nm is observed for Sg-C_3N_4/Bi_2O_3 nanocomposites. In comparison to Sg-C_3N_4/Bi_2O_3 all the Sg-C_3N_4/Bi_2O_3/Ag ternary nanocomposites show a decrease in PL intensity. Moreover, it has been found that with an increase in the wt% of Ag, the PL emission intensity of the ternary composites decreases significantly. This result suggests that the introduction of Ag into the Sg-C_3N_4/Bi_2O_3 composite facilitates the electron–hole pair separation on the surface of the catalyst and with an increase in the amount of Ag the charge carrier separation efficiency increases to a large extent. This may be the sole factor for the improved photocatalytic properties of the ternary nanocomposites containing higher wt% of Ag. This result is well supported by impedance studies and catalytic activity.

3.3.2. DRS study. The optical absorption behaviour of photocatalytic materials plays a major role in the photocatalytic degradation of contaminants, and in order to understand the optical properties we performed UV-Vis DRS analysis of Sg-C_3N_4, Bi_2O_3, Sg-C_3N_4/Bi_2O_3, and Sg-C_3N_4/Bi_2O_3/Ag ternary nanocomposites. Fig. 4 shows the UV-Vis DRS spectra of the prepared nano-photocatalysts. From the figure it is observed that Sg-C_3N_4 shows an absorbance edge in the visible region between 400 and 650 nm which originates from the intrinsic band gap transition of Sg-C_3N_4. In the case of Bi_2O_3, a stiff absorption edge located below 530 nm is observed. The band gaps of Sg-C_3N_4 and Bi_2O_3 are calculated from the Tauc plot and are found to be 2.50 eV and 2.65 eV, respectively. However, after introduction of Bi_2O_3 on Sg-C_3N_4, the resultant binary composite Sg-C_3N_4/Bi_2O_3 shows strong absorbance ranging from the UV to near visible zone with its absorption edge at 620 nm. Compared with Sg-C_3N_4/Bi_2O_3, the prepared Sg-C_3N_4/Bi_2O_3/Ag ternary nanocomposite shows a new absorption peak from 550 to 800 nm, which is due to the surface plasmon resonance (SPR) effect of Ag nanoparticles. The SPR phenomenon is greatly effective in the photocatalysis process as it extends the light absorption properties of the material to visible light. Again, it could be found that the absorbance of Sg-C_3N_4/Bi_2O_3/Ag increases with an increase in the Ag content from 5 to 20%, which further confirms the formation of a ternary nanocomposite containing plasmonic Ag nanoparticles which shows strong absorbance in the entire visible region.

3.4. Morphology analysis

3.4.1. SEM analysis. The surface morphologies and microstructures of prepared Sg-C_3N_4, Sg-C_3N_4/Bi_2O_3 and Sg-C_3N_4/Bi_2O_3/Ag (15%) nanocomposites were analysed using an FESEM (field emission scanning electron microscope) and the obtained images are shown in Fig. 5. Pure Sg-C_3N_4 displays an irregular morphology with loosely organized wrinkled sheets (Fig. 5a). When Bi_2O_3 is introduced into Sg-C_3N_4, the rod shaped submicron Bi_2O_3 particles are randomly distributed on the surface of Sg-C_3N_4 forming a Sg-C_3N_4/Bi_2O_3 hetero-junction (Fig. 5c). But when both Bi_2O_3 and Ag are simultaneously introduced into the

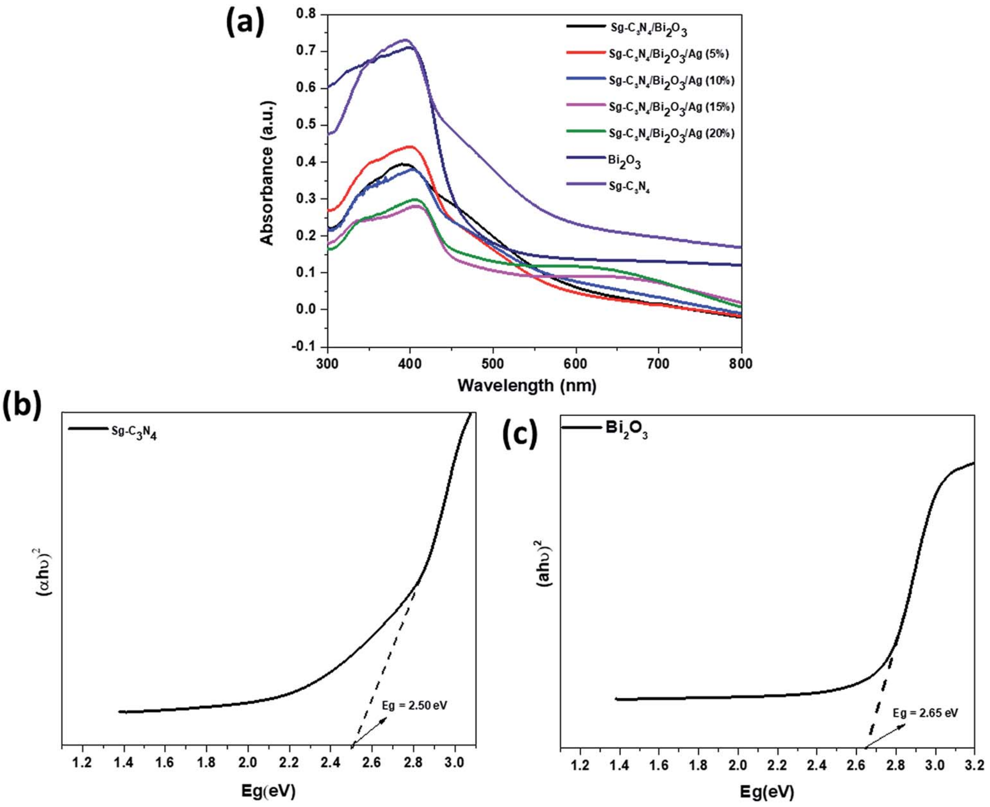

Fig. 4 (a) UV-Vis DRS of Sg-C_3N_4, Bi_2O_3, Sg-C_3N_4, Sg-C_3N_4/Bi_2O_3, Sg-C_3N_4/Bi_2O_3/Ag composites. Band gap energy of (b) Sg-C_3N_4 and (c) Bi_2O_3.

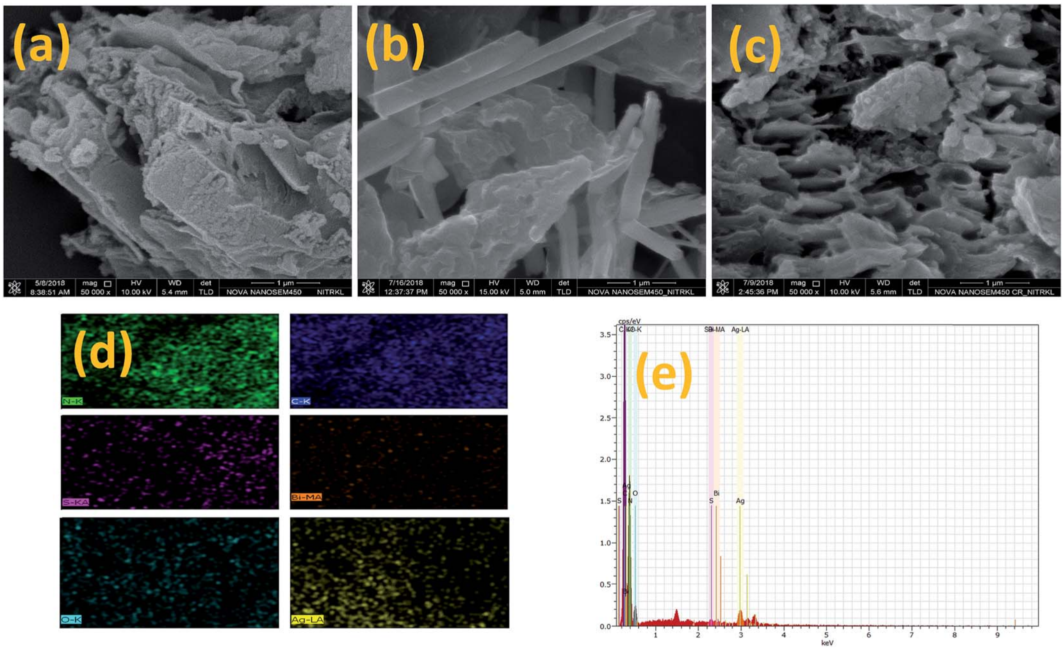

Fig. 5 FESEM images of (a) Sg-C_3N_4, (b) Sg-C_3N_4/Bi_2O_3, and (c) Sg-C_3N_4/Bi_2O_3/Ag (15%); (d) elemental mapping of Sg-C_3N_4/Bi_2O_3/Ag (15%); (e) FESEM EDX spectra of Sg-C_3N_4/Bi_2O_3/Ag (15%).

surface of Sg-C_3N_4, it is interesting to note that the morphology of Bi_2O_3 changed from a rod shape to an irregular shape which may be due to the size depression effect of Ag, Bi_2O_3 and Sg-C_3N_4 as reported in the previous literature.[40,49–51] Further the elemental content of the ternary composite is characterised *via* EDX (Fig. 5d and e), which reveals that it is composed of S, C, N, Bi and O elements and is free from other foreign elements. The obtained results show good correlation with XPS data, discussed in the respective section.

3.4.2. TEM analysis. For further investigation of the particle size distribution, morphology, and crystalline properties of Ag and Bi_2O_3 particles formed on the surface of the 2D layered structure of Sg-C_3N_4 and also for confirmation of the heterojunction, we carried out TEM and HRTEM analysis. Fig. 6 shows the TEM images of Sg-C_3N_4/Bi_2O_3/Ag (15%) ternary nanocomposites. It is observed from the TEM image (Fig. 6a) that spherical Ag nanoparticles and irregular shaped Bi_2O_3 particles are decorated on the Sg-C_3N_4 2D nanosheet surface. The size of the Ag nanoparticles is found to be in the range of 5–10 nm and that of irregular shaped Bi_2O_3 particles is within 80–120 nm, and the particles are well distributed on the surface of 2D sheets of Sg-C_3N_4. Further, from the HRTEM images (Fig. 6d–f) the measured lattice spacings of 0.23 nm and 0.325 nm correspond to the (111) plane of Ag (JCPDS 40783) and the (−120) plane of Bi_2O_3 (JCPDS 14-0699), respectively. However, no crystal plane corresponding to Sg-C_3N_4 is observed, which is due to its organic nature which causes quick weakening of the developing crystal fringes under electron beam irradiation.[52] The TEM elemental analysis further confirms the existence of Ag, Bi, S, C, and N elements. This result suggests the formation of the heterostructure ternary Sg-C_3N_4/Bi_2O_3/Ag nanocomposite.

3.5. XPS analysis

In order to determine the surface composition and chemical states of various elements present in the ternary nanocomposite Sg-C_3N_4/Bi_2O_3/Ag (15%), we performed XPS analysis and the result obtained is depicted in Fig. 7. Fig. 7a shows the high-resolution spectra of C 1s with two peaks at 283.9 and 287 eV, where the former corresponds to the sp^2 hybridised C in the N-heterocyclic aromatic ring (N–C=N) of Sg-C_3N_4 (ref. 35) and the latter is assigned to the adventitious carbon on the sample surface[53]. The peak de-convolution of the N 1s spectrum generates three different peaks (Fig. 7b). The peak at 397.8 eV is ascribed to the carbon atoms bonded to sp^2 hybridised aromatic N atoms (C–N=C),[54] while the component at 398.9 eV usually relates to the bonding of tertiary N atoms to the adjacent carbon atoms in the form of N–$(C)_3$. The weak peaks at 400.5 eV correspond to the bonding of sp^2 nitrogen atoms to three carbon atoms in aromatic rings.[55] In the O 1s spectrum (Fig. 7c), the peak located at 530.8 eV is assigned to the HO–C=O bond and the peak at 529.12 eV is attributed to the Bi–O–Bi bond present in the ternary nanocomposite.[40] Again S 2p is fitted into two peaks (Fig. 7d). The peaks at 163.5 and 166.5 eV indicate the formation of C–S and N–S bonds by substitution of sulphur with nitrogen and carbon of the g-C_3N_4 lattice.[56] In Fig. 7e, two peaks for trivalent Bi (Bi^{3+}) positioned at 157.9 and 163.0 eV are observed, which are assigned to Bi $4f_{5/2}$ and Bi $4f_{7/2}$, respectively.[40] In the Ag 3d XPS spectra shown in Fig. 7f two peaks centred at 367.8 and 373.51 eV are observed. These peaks indicate the binding energy value of Ag $3d_{5/2}$ and Ag $3d_{3/2}$, respectively. This suggests that the Ag is present in its zero oxidation state in the synthesised ternary nanocomposite.[57]

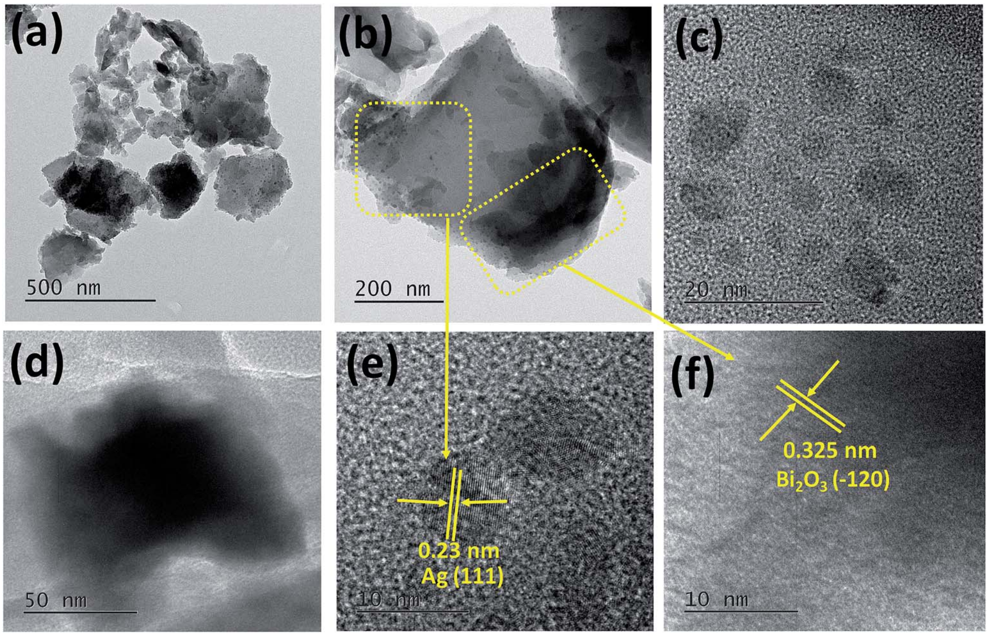

Fig. 6 (a) TEM image of Sg-C_3N_4/Bi_2O_3/Ag (15%). (b) High-resolution TEM image of a selected area of Sg-C_3N_4 in the composite. (c and d) Distribution of Ag nanoparticles and irregular shaped Bi_2O_3 particles on the surface of Sg-C_3N_4. (e and f) Lattice fringes of Ag and Bi_2O_3.

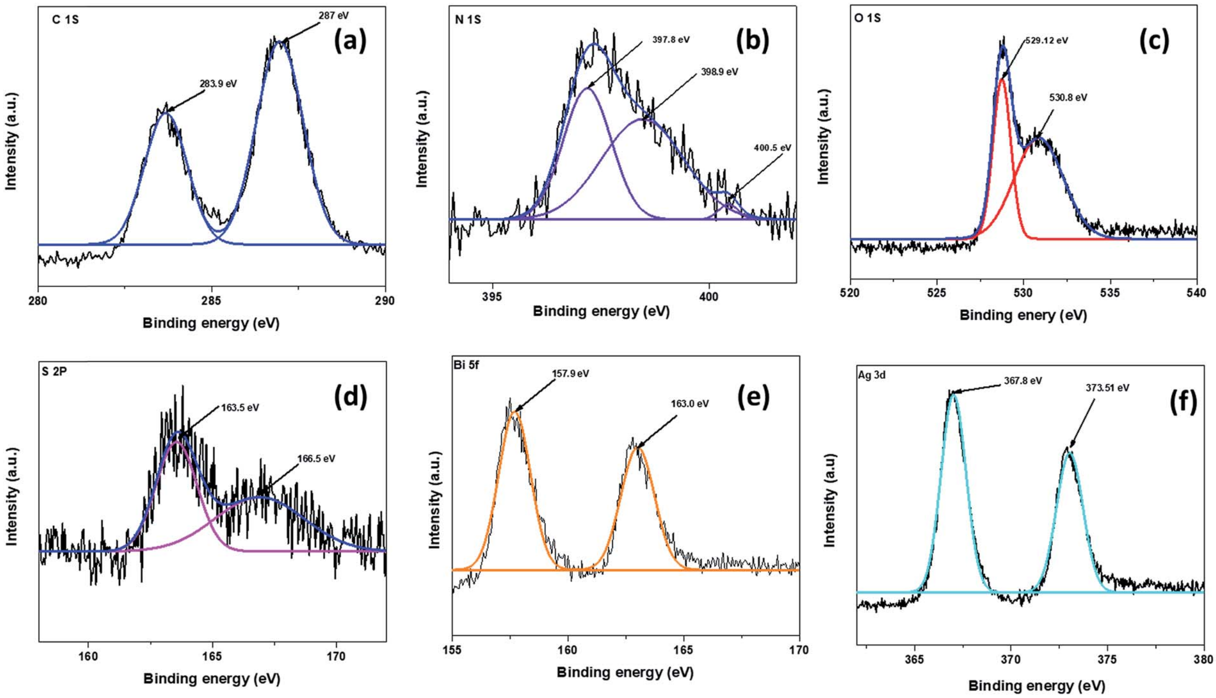

Fig. 7 XPS spectra for Sg-C_3N_4/Bi_2O_3/Ag (15%) in the regions of (a) C 1s, (b) N 1s, (c) O 1s, (d) S 2p, (e) Bi 4f, and (f) Ag 3d.

3.6. Impedance study

Furthermore, to obtain more information regarding the photogenerated electron hole pair separation and charge transfer across the electrode–electrolyte interface of the fabricated ternary photocatalysts we carried out electrochemical impedance (EIS) measurements. Fig. 8 shows the typical Nyquist plots of Sg-C_3N_4, Sg-C_3N_4/Bi_2O_3 and Sg-C_3N_4/Bi_2O_3/Ag (15%) measured in the dark at zero applied bias between 105 and 102 Hz. The semi-circular part in the higher frequency zone indicates the interfacial charge transfer resistance *i.e.* a larger Nyquist arc radius means higher resistance at the interface, and hence lower conductance and *vice versa*. A smaller semicircle in

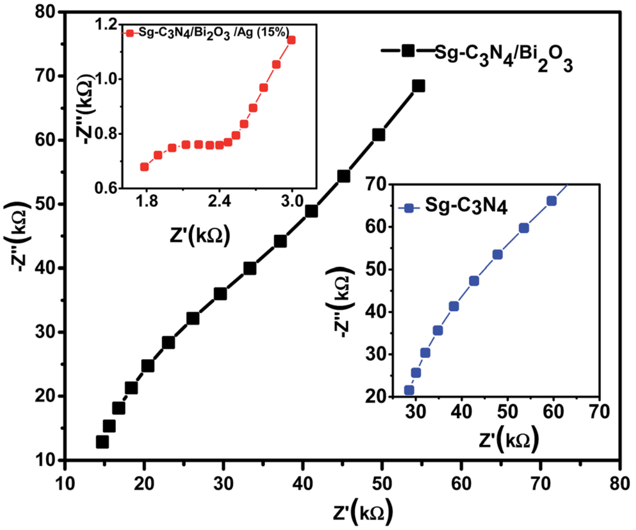

Fig. 8 EIS Nyquist plots of Sg-C_3N_4, Sg-C_3N_4/Bi_2O_3, and Sg-C_3N_4/Bi_2O_3/Ag (15%).

the high frequency zone of the Nyquist plot suggests higher separation efficiency of the photogenerated charge carriers. From the EIS study it is clearly observed that the Sg-C_3N_4/Bi_2O_3/Ag (15%) nanocomposite photocatalyst displays better photogenerated charge carrier separation and transfer efficiency compared to Sg-C_3N_4 and Sg-C_3N_4/Bi_2O_3 photocatalysts. From the above experimental observation it is well understood that the Sg-C_3N_4/Bi_2O_3/Ag (15%) ternary nanocomposite can be effectively used as a photocatalyst with improved photocatalytic degradation activity for organic pollutants.

3.7. Photocatalytic activity

In order to examine the photocatalytic behaviour of the synthesized ternary nanocomposite materials, we used rhodamine B (RhB) dye as a model pollutant and its photocatalytic degradation study was performed under natural solar light. Photocatalytic experiments were carried out by using 60 mg of photocatalyst in 70 ml of 15 ppm RhB solution. Since RhB is a coloured compound and can undergo photolysis under solar light irradiation, we performed blank experiments without using the photocatalyst. A very negligible decolourisation effect was observed in this case which clearly indicates that the deterioration of RhB is only due to the photocatalytic properties of the synthesized photocatalysts. Fig. 9a–c show the photocatalytic decolourization of RhB dye in the presence of the prepared photocatalysts. It was observed that for all the samples the rate of decolourisation increases with time. In order to further examine the effect of adsorption on the decolourisation process, we also performed an adsorption experiment in the dark with a contact time of 90 min keeping all parameters and adsorbent dose constant. It was found that only 3% of the RhB solution gets adsorbed onto the catalyst surface. The results for the decolourisation of RhB by various prepared photocatalysts are presented in Fig. 9a. It is observed from the figure that the photocatalytic efficiency of the Sg-C_3N_4/Bi_2O_3 nanocomposite in RhB decolourisation is only about 10.25%. So in order to further improve the photocatalytic properties we tried to modify Sg-C_3N_4/Bi_2O_3 nanocomposites by decorating them with various amounts of Ag nanoparticles. It is found that with an increase in Ag content from 5 wt% to 15 wt% the photocatalytic performance of the resultant ternary nanocomposite increases gradually and then decreases slightly for 20 wt% Ag. Among all the prepared nanocomposites Sg-C_3N_4/Bi_2O_3/Ag (15%) shows 95% degradation ability which is significantly higher than that of other prepared nanocomposites. The order of decolourisation efficiency of the prepared nanocomposites is found to be Sg-C_3N_4/Bi_2O_3/Ag (15%) > Sg-C_3N_4/Bi_2O_3/Ag (20%) > Sg-C_3N_4/Bi_2O_3/Ag (10%) > Sg-C_3N_4/Bi_2O_3/Ag (5%) > Sg-C_3N_4/Bi_2O_3. The decrease in photocatalytic ability with an increase in wt% of Ag from 15% to 20% might be due to the agglomeration of Ag nanoparticles in the presence of higher Ag content. These agglomerated nanoparticles block the active sites of the composites and decrease the electron–hole pair separation efficiency. Thus the content of Ag in the ternary nanocomposite plays a very important role in determining the photocatalytic ability. Moreover, we also studied the kinetics of the degradation of RhB dye by the prepared ternary nanocomposites and the experimental data obtained are found to be best fitted to the kinetic model of a pseudo-first order reaction (Fig. 9b). The pseudo-first order kinetic equation is presented below

$$\ln(C/C_0) = kt \tag{1}$$

where C is the final concentration at time t and C_0 is the initial concentration, and the slope of the plot of $\ln(C/C_0)$ *vs.* the irradiation time (t) gives the value of k or k_{app} which is called the pseudo first order rate constant or apparent rate constant. The k values for different samples are shown in Fig. 9c and also in Table S1.† It is found from Table S1† that the Sg-C_3N_4/Bi_2O_3/Ag (15%) ternary nanocomposite photocatalyst shows much higher photocatalytic efficiency than other prepared nanocomposites which can be ascribed to the best synergistic interaction between the ternary phases, better visible light absorption capability, and higher photogenerated electron–hole charge separation ability compared to other synthesized nanocomposites.

Furthermore, it is known that coloured dye solution affects the photocatalytic properties of catalysts to a great extent through the photosensitization effect. Therefore, in order to examine the intrinsic photocatalytic efficiency of all the synthesized ternary nanocomposites for broader application, we also tested their photocatalytic performance towards the degradation of 10 ppm TCH solution under natural sunlight. The procedure for TCH degradation and experimental conditions were maintained identical to those of RhB. Fig. 9d presents the rate of degradation of TCH as a function of time. Fig. 9e and f present the TCH degradation kinetics and the value of rate constant (k_{app}) for different photocatalysts during the first cycle of the experiment. It is clearly seen that Sg-C_3N_4/Bi_2O_3 degrades only 47.8% of TCH under 60 min illumination of sunlight. While with respect to Sg-C_3N_4/Bi_2O_3/Ag (5%), Sg-C_3N_4/Bi_2O_3/Ag (10%), Sg-C_3N_4/Bi_2O_3/Ag (15%) and Sg-C_3N_4/Bi_2O_3/Ag (20%), the

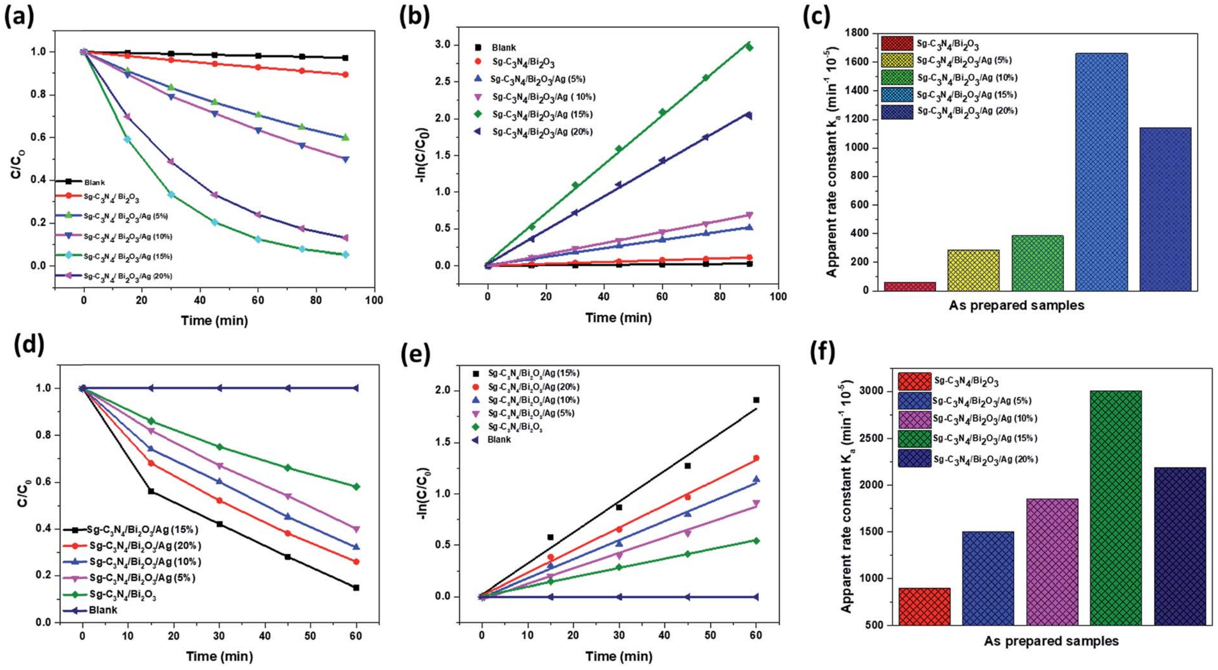

Fig. 9 (a) Photocatalytic decolourisation plots of RhB under natural sunlight, (b) first order kinetic study of RhB degradation, (c) apparent rate constant of the materials for RhB degradation, (d) photocatalytic degradation plots of TCH under natural sunlight, (e) first order kinetic study of TCH degradation, and (f) apparent rate constant of the materials for TCH degradation.

degradation percentages of TCH are 60%, 68%, 85.18% and 74.08%, respectively, under the same reaction conditions. From this result (Table S1†), it can be concluded that in comparison to other prepared ternary nanocomposites, $SgC_3N_4/Bi_2O_3/Ag$ (15%) shows better photocatalytic ability towards the degradation of TCH under solar light. This study provides conclusive proof that the catalytic behaviour is only due to the photocatalytic ability of the ternary nanocomposites, even though some minimal sensitization effect is observed as in the case of RhB, but that can be ignored.

3.8. Determination of reactive species involved in the decolourisation process

In the semiconductor based photocatalysis process electrons (e^-), holes (h^+), hydroxyl radicals ($^{\bullet}OH$), superoxide radicals ($^{\bullet}O_2^-$) *etc.* are the main reactive species that are basically generated and are involved in the degradation of harmful organic pollutants. So for examining the main reactive species involved in the decolourisation process, we performed decolourization of RhB dye in the presence of different scavenger solutions (1 mM). The result of the scavenger study obtained with the Sg-C_3N_4/Bi_2O_3/Ag (15%) nanocomposite photocatalyst is presented in Fig. 10a. From this figure it is seen that when *para*-benzoquinone is used as the scavenger, 36.48% decolourisation of RhB is observed which signifies that superoxide radicals play a role in the degradation process. However, when *tert*-butyl alcohol and EDTA are used, which are generally used to trap hydroxyl radicals and holes, the decolourization rate decreases significantly. This result suggests that both hydroxyl radicals and holes play a major role in the decolourisation process. Again, when DMSO is used as a scavenger for electrons the result shows that 34.37% of RhB solution is decolourised which suggests that electrons are also important reactive species involved in the process of degradation (Table S2†). Therefore, from the above experimental findings it is concluded that the roles of various reactive species in the RhB decolourisation process are in the following order: $h^+ > {}^{\bullet}OH > e^- > {}^{\bullet}O_2^-$.

In order to further support the scavenger study, we also carried out a confirmatory test for the formation of hydroxyl and superoxide radicals during the photocatalytic reaction process. For hydroxyl radicals, a terephthalic acid (TA) assisted PL spectroscopy technique was used in which TA solution was used to trap the photogenerated $^{\bullet}OH$ radicals which form highly fluorescent 2-hydroxyterephthalic acid (TAOH). Thus the fluorescence intensity of 2-hydroxyterephthalic acid can be correlated with the concentration of $^{\bullet}OH$ generated during the reaction process. From Fig. 10b and c, it is clear that for Sg-C_3N_4, Sg-C_3N_4/Bi_2O_3 and Sg-C_3N_4/Bi_2O_3/Ag (15%) the fluorescence intensity of TAOH gradually increases, suggesting that for all three samples the generation of $^{\bullet}OH$ increases with an increase in illumination time. As the VB (valence band) potential for Sg-C_3N_4 is +1.23 eV (*vs.* NHE) and the CB potential is −1.27 eV (*vs.* NHE), the holes present in the VB of Sg-C_3N_4 cannot oxidise directly OH^- to $^{\bullet}OH$ ($^{\bullet}OH/OH^- = +1.99$ eV *vs.* NHE). Hence the $^{\bullet}OH$ must be produced in an indirect manner, by the reaction of protons with $^{\bullet}O_2^-$. Again as the CB potential of Sg-C_3N_4 is more negative than the $O_2/^{\bullet}O_2^-$ (−0.33 eV *vs.* NHE) reduction potential these $^{\bullet}O_2^-$ radical species were produced by means of single electron reduction of surface adsorbed O_2 molecules. However, in the case of the Sg-C_3N_4/Bi_2O_3

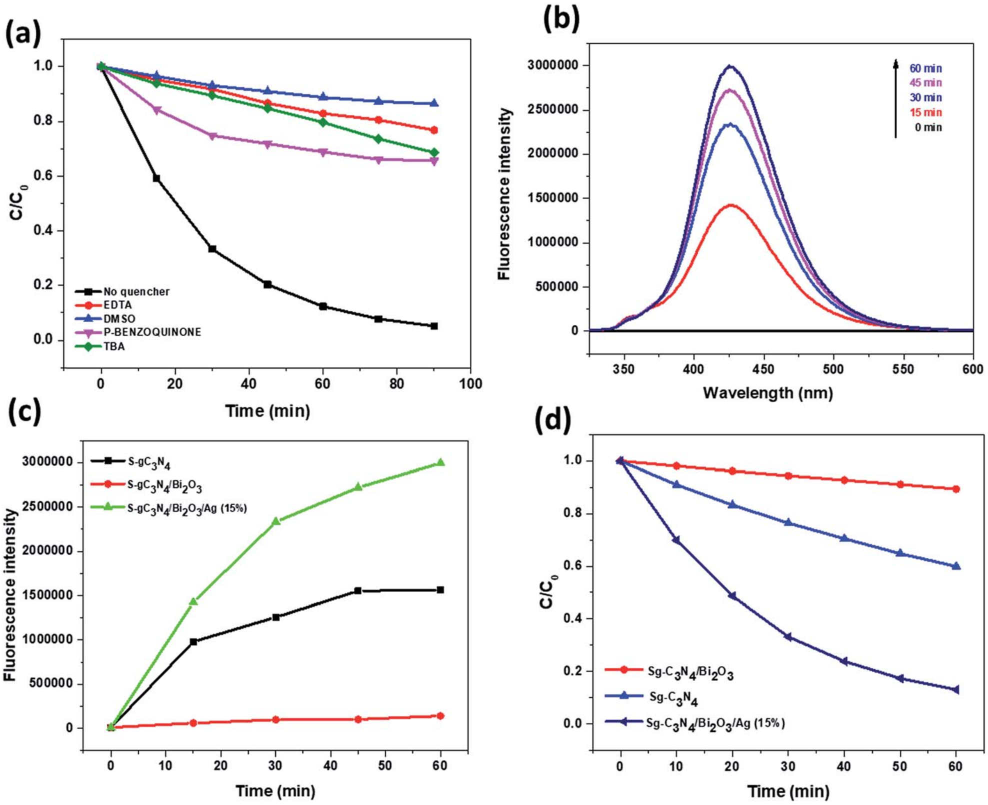

Fig. 10 (a) Photodecolorization of RhB by the $SgC_3N_4/Bi_2O_3/Ag$ (15%) composite in the presence of different scavengers, (b) fluorescence spectra of 3-hydroxyterephthalic acid formed at different irradiation times in aqueous suspension of the $SgC_3N_4/Bi_2O_3/Ag$ (15%) catalyst, (c) comparison of the PL intensity with time for Sg-C_3N_4, SgC_3N_4/Bi_2O_3 and $SgC_3N_4/Bi_2O_3/Ag$ (15%) materials, and (d) rate of reduction of NBT with time by Sg-C_3N_4, SgC_3N_4/Bi_2O_3 and $SgC_3N_4/Bi_2O_3/Ag$ (15%).

nanocomposite, as the VB potential of Bi_2O_3 is more positive than that of Sg-C_3N_4 the photogenerated holes on the surface of Bi_2O_3 will be transferred to Sg-C_3N_4. Meanwhile, the electrons generated on the surface of Sg-C_3N_4 will be transferred to Bi_2O_3, because the CB potential of Bi_2O_3 is less negative than that of Sg-C_3N_4. But as the CB potential of Bi_2O_3 is +0.40 eV (*vs.* NHE), which is too low to reduce O_2 to $^{\bullet}O_2^-$, the formation of $^{\bullet}O_2^-$ radical species by the reduction of surface adsorbed O_2 molecules is restricted. This suggests that the formation of $^{\bullet}OH$ in the case of Sg-C_3N_4/Bi_2O_3 in both a direct and indirect manner is quite low which is clear from the experimental results. Furthermore, in the case of the Sg-$C_3N_4/Bi_2O_3/Ag$ (15%) ternary nanocomposite, owing to the incorporation of Ag into the Sg-C_3N_4/Bi_2O_3 nanocomposite system, the amount of $^{\bullet}OH$ produced is the most significant. This is because the metallic Ag^0 sites which act as an electron pool transfer the photoexcited electrons from Sg-C_3N_4 and reduce the O_2 to $^{\bullet}O_2^-$ which again combines with protons and subsequently forms $^{\bullet}OH$ radicals.

Again, in order to obtain conclusive evidence of the formation of $^{\bullet}O_2^-$ species in the reaction system, we performed an NBT test under visible light illumination conditions for 1 h. In the NBT test, the reagent nitroblue tetrazolium chloride (NBT) was used as a molecular probe for the detection of superoxide radical ($^{\bullet}O_2^-$) species. It is well known that NBT gets reduced selectively by superoxide radicals ($^{\bullet}O_2^-$) and forms formazan, which can be detected from the decrease in NBT absorption intensity with the progress of illumination time. The obtained result is presented in Fig. 10d. It is found that the formation of $^{\bullet}O_2^-$ species is the highest for the Sg-$C_3N_4/Bi_2O_3/Ag$ (15%) ternary nanocomposite among other prepared photocatalysts. Again from the result of the terephthalic acid test and NBT test it can be concluded that the extent of $^{\bullet}OH$ formation depends upon the amount of $^{\bullet}O_2^-$ species produced during the reaction process, and thus the $^{\bullet}OH$ species in the reaction system are produced indirectly from $^{\bullet}O_2^-$.

3.9. Possible mechanism for photodegradation activity of the Sg-$C_3N_4/Bi_2O_3/Ag$ nanocomposite

From the obtained experimental results, we have proposed a mechanistic pathway for the photocatalytic activity of the synthesized ternary nanocomposite (Scheme 2). From the UV-Vis DRS study the band gap for Sg-C_3N_4 and Bi_2O_3 is estimated to be 2.50 eV and 2.65 eV, respectively. This reflects that both Sg-C_3N_4 and Bi_2O_3 components of the composite can absorb visible light. The VB and CB potentials for Sg-C_3N_4 and Bi_2O_3 are calculated by using the following equations:

$$E_{VB} = X - E_e + 0.5E_g \quad (2)$$

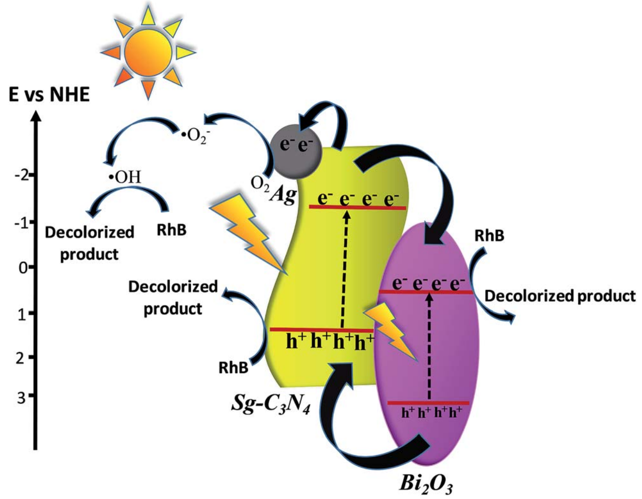

Scheme 2 Proposed mechanism for RhB decolourization by the Sg-$C_3N_4/Bi_2O_3/Ag$ ternary photocatalyst.

$$E_{CB} = E_{VB} - E_g \tag{3}$$

where E_g represents the band gap energy, and E_{VB} and E_{CB} are the valence band and conduction band edge potentials (*vs.* NHE). E_e represents the free electron energy on the hydrogen scale (4.5 eV) and X is the absolute electronegativity of the respective semiconductor material. The X values for Sg-C_3N_4 and Bi_2O_3 are 4.48 and 6.23 eV, respectively. On the basis of the above formulae the positions of the conduction band and valence band for Sg-C_3N_4 and Bi_2O_3 are depicted in Scheme 2. According to the band gap alignment, since the conduction band potential of Sg-C_3N_4 (−1.27 eV *vs.* NHE) was more negative than that of Bi_2O_3 (+0.4 eV *vs.* NHE), the photogenerated electrons will migrate from the CB of Sg-C_3N_4 to the CB of Bi_2O_3. As the $O_2/{}^{\bullet}O_2^-$ reduction potential is −0.33 eV *vs.* NHE, the electrons accumulated on the CB band of Bi_2O_3 cannot reduce surface adsorbed O_2 to ${}^{\bullet}O_2^-$ and hence these electrons directly participate in the reduction of RhB. But in the case of Sg-$C_3N_4/Bi_2O_3/Ag$ (15%), some of the electrons which are present in the CB of Sg-C_3N_4, due to photo-excitation of its valence band electrons, get transferred to the O_2 molecules *via* the attached Ag^0 sites to produce ${}^{\bullet}O_2^-$ radical species. But from the scavenger study it is confirmed that in comparison to ${}^{\bullet}O_2^-$, ${}^{\bullet}OH$ plays a major role in the decolourisation process. This suggests that these ${}^{\bullet}O_2^-$ species formed yet again react with protons to produce H_2O_2 which is further transformed to ${}^{\bullet}OH$. Moreover, it is worth noting that the VB of Sg-C_3N_4 (+1.23 eV *vs.* NHE) is located above the valence band of Bi_2O_3 (+3.05 eV *vs.* NHE) which forms a unique band arrangement that efficiently facilitates the gradual and smooth transfer of photo-induced holes from Bi_2O_3 to Sg-C_3N_4 *via* the intermediate hetero-junction created between them. The redox potential of $OH^-/{}^{\bullet}OH$ (1.99 eV *vs.* NHE) is more positive with respect to the redox potential of the VB holes of Sg-C_3N_4, which indicates that the holes on the valence band of Sg-C_3N_4 would react with RhB directly. Therefore, it is observed that all the active species generated in the reaction system play a significant role in the decolourisation of RhB. The possible reactions that are involved in the photo-decolourisation process are listed below.

$$\text{Sg-}C_3N_4/Bi_2O_3/Ag + h\nu \rightarrow \text{Sg-}C_3N_4\ (e^-\ldots h^+) + Bi_2O_3\ (e^-\ldots h^+)$$

$$\text{Sg-}C_3N_4\ (e^-) + Bi_2O_3 \rightarrow \text{Sg-}C_3N_4 + Bi_2O_3\ (e^-)$$

$$\text{Sg-}C_3N_4\ (e^-) + Ag \rightarrow \text{Sg-}C_3N_4 + Ag\ (e^-)$$

$$Ag\ (e^-) + O_2 \rightarrow {}^{\bullet}O_2^- + Ag$$

$${}^{\bullet}O_2^- + H^+ \rightarrow {}^{\bullet}OOH$$

$${}^{\bullet}OOH + H^+ + Ag\ (e^-) \rightarrow H_2O_2 + Ag$$

$$H_2O_2 + Ag\ (e^-) \rightarrow {}^{\bullet}OH + OH^- + Ag$$

$$Bi_2O_3\ (h^+) + \text{Sg-}C_3N_4 \rightarrow Bi_2O_3 + \text{Sg-}C_3N_4\ (h^+)$$

$$RhB + {}^{\bullet}OH^- + {}^{\bullet}O_2^- + Bi_2O_3\ (e^-) + \text{Sg-}C_3N_4\ (h^+) \rightarrow \text{decolourisation product.}$$

3.10. Evaluation of toxicity of TCH

It is well known that TCH has a strong bacteriostatic effect.[60] So in order to measure the residual toxicity of TCH after photodegradation, *E. coli* was chosen as the model microorganism. Fig. S1† shows the antibacterial activity of TCH after photocatalytic degradation reaction for 0 min, 30 min, and 60 min of light illumination. From the figure it is clearly observed that before light illumination no bacterial colonies are observed which is due to the strong antibacterial activity of TCH molecules. But after photocatalytic reaction for 30 min a few bacterial colonies are observed, which indicates that the toxicity of TCH is decreased compared to pure TCH. At the end of 1 h treatment, the number of bacterial colonies increased further and their size became bigger, suggesting that the toxicity of TCH is eliminated efficiently by using the synthesized ternary nanocomposite photocatalyst.

3.11. Analysis of degradation products of TCH

In order to investigate the photocatalytic degradation products of TCH molecules, we carried out GC-MS analysis of the aliquots taken out at different time intervals (0 min, 30 min, and 60 min) during the photocatalytic reaction. From GC-MS analysis it was observed that the photocatalytic degradation process of TCH molecules proceeds through a complex mechanism and as a result of which various degraded intermediate molecules were formed.[58] During the photocatalytic degradation of TCH, the intermediate molecules formed were due to ring opening, oxidation, and reduction reactions, and as a result of which the formation of numerous polar and nonpolar intermediates with different *m*/*z* values ranging from 73 to 490 was observed. Some of the intermediate compounds identified from the mass spectra, their retention times and possible chemical structures are listed in Table S3.† This experimental study proves that TCH is degraded to smaller organic molecules/intermediates, which may eventually turn into CO_2 and H_2O and other smaller products.[59]

3.12. Reusability of the photocatalyst

For the practical application of the photocatalyst, reusability is a very important factor that must be considered. So in order to determine the stability and reusability of the photocatalyst, recycling experiments for RhB degradation by Sg-C_3N_4/Bi_2O_3/Ag (15%) were performed. The results reveal that there is not much decrease in the catalytic activity even after four successive cycles (Fig. S2†). Moreover, the XRD analyses of used samples were also performed to compare the stability of fresh and used samples. It is found that almost no discrepancy in the phase and structure of the recycled photocatalyst was observed. This illustrates that the prepared photocatalyst presents excellent stability and efficiency.

4. Conclusion

In summary, we have successfully synthesized solar light driven visible light responsive S doped g-C_3N_4/Bi_2O_3/Ag plasmonic photocatalysts, by using facile chemical precipitation followed by a heat treatment process. Among all the synthesized ternary nanocomposites Sg-C_3N_4/Bi_2O_3/Ag (15%) showed enhanced photocatalytic activity towards the decolourisation of RhB dye and degradation of TCH under natural solar light. This result might be due to the better visible light absorption, efficient electron–hole pair separation, and formation of a hetero-junction and synergetic interaction between the nano-sized Ag, irregular shaped Bi_2O_3 and 2D sheets of Sg-C_3N_4 of the ternary nanocomposite. The mechanistic pathway for the degradation of RhB dye was thoroughly investigated by means of scavenger experimental studies and it is found that the effects of various reactive species on the degradation process are in the following order: $h^+ > {}^{\bullet}OH > e^- > {}^{\bullet}O_2^-$. Moreover, from the reusability study it is observed that the synthesized ternary nanocomposite possesses excellent stability and efficiency. This suggests that the synthesized ternary nanocomposite can be effectively used as a heterogeneous solar light responsive photocatalyst for the decomposition of aqueous organic pollutants.

Conflicts of interest

There are no conflicts to declare.

Acknowledgements

The authors would like to acknowledge NIT Rourkela, India (Odisha), for providing the research facility and funding to carry out this work.

References

1 M. Mousavi and A. Habibi-Yangjeh, *J. Colloid Interface Sci.*, 2016, **465**, 83–92.

2 S. Fu, Y. He, Q. Wu, Y. Wu and T. Wu, *J. Mater. Res.*, 2016, **31**, 2252–2260.

3 B. Gupta, A. A. Melvin, T. Matthews, S. Dhara, S. Dash and A. K. Tyagi, *Int. J. Hydrogen Energy*, 2015, **40**, 5815–5823.

4 X. Yan, R. Xu, J. Guo, X. Cai, D. Chen, L. Huang, Y. Xiong and S. Tan, *Mater. Res. Bull.*, 2017, **96**, 18–27.

5 X. She, J. Wu, H. Xu, J. Zhong, Y. Wang, Y. Song, K. Nie, Y. Liu, Y. Yang, M. T. F. Rodrigues, R. Vajtai, J. Lou, D. Du, H. Li and P. M. Ajayan, *Adv. Energy Mater.*, 2017, **7**, 1–7.

6 N. Li, J. Zhang, Y. Tian, J. Zhao, J. Zhang and W. Zuo, *Chem. Eng. J.*, 2017, **308**, 377–385.

7 K. Acuña, J. Yáñez, S. Ranganathan, E. Ramírez, J. Pablo Cuevas, H. D. Mansilla and P. Santander, *Sol. Energy*, 2017, **157**, 335–341.

8 Z. Khodami and A. Nezamzadeh-Ejhieh, *J. Mol. Catal. A: Chem.*, 2015, **409**, 59–68.

9 M. Xu, L. Han and S. Dong, *ACS Appl. Mater. Interfaces*, 2013, **5**, 12533–12540.

10 C. Garkoti, J. Shabir and S. Mozumdar, *New J. Chem.*, 2017, **41**, 9291–9298.

11 Y. Wang, J. Sun, J. Li and X. Zhao, *Langmuir*, 2017, **33**, 4694–4701.

12 X. Cai, H. Liu, L. Zhi, H. Wen, A. Yu, L. Li, F. Chen and B. Wang, *RSC Adv.*, 2017, **7**, 46132–46138.

13 O. Elbanna, M. Fujitsuka and T. Majima, *ACS Appl. Mater. Interfaces*, 2017, **9**, 34844–34854.

14 L. Sun, T. Du, C. Hu, J. Chen, J. Lu, Z. Lu and H. Han, *ACS Sustainable Chem. Eng.*, 2017, **5**, 8693–8701.

15 L. Shi, L. Liang, F. Wang, M. Liu and J. Sun, *Dalton Trans.*, 2016, **45**, 5815–5824.

16 S. Zhang, J. Li, X. Wang, Y. Huang, M. Zeng and J. Xu, *ACS Appl. Mater. Interfaces*, 2014, **6**, 22116–22125.

17 X. Yang, H. Tang, J. Xu, M. Antonietti and M. Shalom, *ChemSusChem*, 2015, **8**, 1350–1358.

18 L. Qu, N. Chen, F. Zhao, C. Hu, Q. Han and Z. Zhang, *J. Mater. Chem. A*, 2015, **3**, 4612–4619.

19 Y. Zhou, L. Zhang, J. Liu, X. Fan, B. Wang, M. Wang, W. Ren, J. Wang, M. Li and J. Shi, *J. Mater. Chem. A*, 2015, **3**, 3862–3867.

20 T. Liu, Y. Wang, Y. Wei, X. Ma, B. Liu, S. Yin, L. Yang, Y. Jing and H. Li, *RSC Adv.*, 2017, **7**, 8688–8693.

21 F. Dong, Z. Zhao, Y. Sun, Y. Zhang, S. Yan and Z. Wu, *Environ. Sci. Technol.*, 2015, **49**, 12432–12440.

22 J. Xue, S. Ma, Y. Zhou, Z. Zhang and M. He, *ACS Appl. Mater. Interfaces*, 2015, **7**, 9630–9637.

23 V. Sharma, S. Kumar and V. Krishnan, *ChemistrySelect*, 2016, **1**, 2963–2970.

24 Y. Li, H. Zhang, P. Liu, D. Wang, Y. Li and H. Zhao, *Small*, 2013, **9**, 3336–3344.

25 Y. Xu, F. Ge, Z. Chen, S. Huang, W. Wei, M. Xie and H. Xu, *Appl. Surf. Sci.*, 2019, **469**, 739–746.

26 Z. Zhu, X. Tang, T. Wang, W. Fan, Z. Liu and C. Li, *Appl. Catal., B*, 2019, **241**, 319–328.

27 M. Zhang, X. Bai, D. Liu, J. Wang and Y. Zhu, *Appl. Catal., B*, 2015, **164**, 77–81.

28 Z. Li, C. Kong and G. Lu, *J. Phys. Chem. C*, 2016, **120**, 56–63.

29 C. Lu, R. Chen, X. Wu, M. Fan, Y. Liu, Z. Le, S. Jiang and S. Song, *Appl. Surf. Sci.*, 2016, **360**, 1016–1022.
30 N. Bao, X. Hu, Q. Zhang, X. Miao, X. Jie and S. Zhou, *Appl. Surf. Sci.*, 2017, **403**, 682–690.
31 K. Wang, Q. Li, B. Liu, B. Cheng, W. Ho and J. Yu, *Appl. Catal., B*, 2015, **176–177**, 44–52.
32 Y. Zhu, T. Ren and Z. Yuan, *ACS Appl. Mater. Interface*, 2015, **7**, 16850–16856.
33 B. Zhu, J. Zhang, C. Jiang, B. Cheng and J. Yu, *Appl. Catal., B*, 2017, **207**, 27–34.
34 S. C. Smith, G. Liu, Z. Chen, G. Q. Lu, H.-M. Cheng, P. Niu and C. Sun, *J. Am. Chem. Soc.*, 2010, **132**, 11642–11648.
35 L. Jiang, X. Yuan, G. Zeng, X. Chen, Z. Wu, J. Liang, J. Zhang, H. Wang and H. Wang, *ACS Sustainable Chem. Eng.*, 2017, **5**, 5831–5841.
36 K. Wang, Q. Li, B. Liu, B. Cheng, W. Ho and J. Yu, *Appl. Catal., B*, 2015, **176–177**, 44–52.
37 J. Liu, *J. Phys. Chem. C*, 2015, **119**, 28417–28423.
38 W. Cui, Y. Liang, W. An, L. Liu, Y. Qi, J. Lu and S. Lin, *Appl. Catal., B*, 2015, **183**, 133–141.
39 R. He, J. Zhou, H. Fu, S. Zhang and C. Jiang, *Appl. Surf. Sci.*, 2018, **430**, 273–282.
40 H. Y. Jiang, G. Liu, T. Wang, P. Li, J. Lin and J. Ye, *RSC Adv.*, 2015, **5**, 92963–92969.
41 D. He, X. Hou, S. Xue, W. Xie and X. Wei, *Mater. Lett.*, 2015, **161**, 640–643.
42 P. Qiu, C. Han, W. Liu, X. Li, L. Ge and S. Fang, *Appl. Catal., B*, 2015, **176–177**, 62–69.
43 C. Liu, C. Cao, X. Luo and S. Luo, *J. Hazard. Mater.*, 2015, **285**, 319–324.
44 B. Cheng, N. Wu, J. Yu, A. Meng, S. Song and S. Cao, *Appl. Catal., B*, 2015, **181**, 71–78.
45 Q. Xu, C. Jiang, B. Zhu, B. Cheng and J. Yu, *Sol. RRL*, 2018, **2**, 1800006.
46 J. Zhang, Y. Hu, X. Jiang, S. Chen, S. Meng and X. Fu, *J. Hazard. Mater.*, 2014, **280**, 713–722.
47 S. Martha, S. Mansingh, K. M. Parida and A. Thirumurugan, *Mater. Chem. Front.*, 2017, **1**, 1641–1653.
48 Z. Zhu, Y. Yu, H. Dong, Z. Liu, C. Li, P. Huo and Y. Yan, *ACS Sustainable Chem. Eng.*, 2017, **5**, 10614–10623.
49 J. Li, J. Yan, B. Chai, L. Hu and C. Wang, *Appl. Surf. Sci.*, 2017, **430**, 243–252.
50 X. Liu, J. Liu, H. Chu, J. Li, W. Yu, G. Zhu, L. Niu, Z. Sun, L. Pan and C. Q. Sun, *Appl. Surf. Sci.*, 2015, **347**, 269–274.
51 H. Y. Jiang, G. Liu, P. Li, D. Hao, X. Meng, T. Wang, J. Lin and J. Ye, *RSC Adv.*, 2014, **4**, 55062–55066.
52 S. Sun, M. Sun, Y. Kong, F. Liu, Z. Yu and S. Anandan, *J. Mater. Sci.*, 2017, **52**, 1183–1193.
53 H. T. Ren, S. Y. Jia, Y. Wu, S. H. Wu, T. H. Zhang and X. Han, *Ind. Eng. Chem. Res.*, 2014, **53**, 17645–17653.
54 T. Liu, Y. Wang, Y. Wei, X. Ma, B. Liu, S. Yin, L. Yang, Y. Jing and H. Li, *RSC Adv.*, 2017, **7**, 8688–8693.
55 Z. Wang, Y. Dai, K. Li, B. Huang, J. Lu, S. Gao, Q. Wang and H. Xu, *ACS Appl. Mater. Interfaces*, 2015, **7**, 9023–9030.
56 M. Jourshabani, Z. Shariatinia and A. Badiei, *J. Colloid Interface Sci.*, 2017, **507**, 59–73.
57 Y. Zhang, J. Wu, Y. Deng, Y. Xin, H. Liu, D. Ma and N. Bao, *Mater. Sci. Eng., B*, 2017, **221**, 1–9.
58 A. C. Martins, A. L. Cazetta, O. Pezoti, J. R. B. Souza and T. Zhang, *Ceram. Int.*, 2017, **43**, 4411–4418.
59 X. Zhu, Y. Wang, R. Sun and D. Zhou, *Chemosphere*, 2013, **92**, 925–932.
60 Y. Xu, J. Liu, M. Xie, L. Jing, J. Yan, J. Deng, H. Xu, H. Li and J. Xie, *Inorg. Chem. Front.*, 2018, **5**, 2818.